

ALMA OBSERVATIONS OF THE T TAURI BINARY SYSTEM AS 205: EVIDENCE FOR MOLECULAR WINDS AND/OR BINARY INTERACTIONS

COLETTE SALYK¹, KLAUS PONTOPPIDAN², STUARTT CORDER³, DIEGO MUÑOZ⁴, KE ZHANG⁵, AND GEOFFREY A. BLAKE⁵

¹ National Optical Astronomy Observatory, 950 North Cherry Avenue, Tucson, AZ 85719, USA; csalyk@noao.edu

² Space Telescope Science Institute, 3700 San Martin Drive, Baltimore, MD 21218, USA

³ Joint ALMA Observatory, Av. Alonso de Córdova 3107, Vitacura, Santiago, Chile

⁴ Center for Space Research, Department of Astronomy, Cornell University, Ithaca, NY 14853, USA

⁵ Division of Geological and Planetary Sciences, Mail Code 150-21, California Institute of Technology, Pasadena, CA 91125, USA

Received 2013 December 21; accepted 2014 July 3; published 2014 August 18

ABSTRACT

In this study, we present high-resolution millimeter observations of the dust and gas disk of the T Tauri star AS 205 N and its companion, AS 205 S, obtained with the Atacama Large Millimeter Array. The gas disk around AS 205 N, for which infrared emission spectroscopy demonstrates significant deviations from Keplerian motion that has been interpreted as evidence for a disk wind, also displays significant deviations from Keplerian disk emission in the observations presented here. Detections near both AS 205 N and S are obtained in 1.3 mm continuum, ^{12}CO 2–1, ^{13}CO 2–1, and C^{18}O 2–1. The ^{12}CO emission is extended up to $\sim 2''$ from AS 205 N, and both ^{12}CO and ^{13}CO display deviations from Keplerian rotation at all angular scales. Two possible explanations for these observations hold up best to close scrutiny—tidal interaction with AS 205 S or disk winds (or a combination of the two)—and we discuss these possibilities in some detail.

Key words: protoplanetary disks – stars: protostars

Online-only material: color figures

1. INTRODUCTION

Observations of protoplanetary disks—the birthplace of planets—provide a window into the processes by which planets form. While the dust component of protoplanetary disks has historically been easier to observe, the gas component contains the bulk of the disk mass and encodes much of the important disk physics and chemistry. Therefore, obtaining observations of the disk gas remains an important goal, in spite of its challenges. To date, the majority of molecular gas detections in disks have come from infrared (IR) observations, where the heated disk atmospheres in the inner parts of disks (typically within ~ 5 AU) produce emission from rovibrational or high-energy pure rotational molecular transitions (e.g., Najita et al. 2003; Pontoppidan et al. 2010). Considerably fewer observations have been obtained of disk gas from the outer parts of disks, especially observations of the lowest-energy pure rotational transitions at millimeter wavelengths, as the sensitivity of current instruments allowed for the high-resolution study of only the brightest protoplanetary disks (e.g., Dutrey et al. 1997; Simon et al. 2000; Öberg et al. 2010). Yet it is the combination of observations across a wide range of wavelengths, probing a wide range of disk radii, that will enable a more complete understanding of disks.

This situation is about to change dramatically, as the superior sensitivity and image quality provided by the Atacama Large Millimeter Array (ALMA) are enabling extensive observations of disk gas at millimeter wavelengths. In particular, ALMA observations will allow for detailed studies of its motion and distribution. Indeed, ALMA observations have already revealed gaseous flows across a disk cavity (Casassus et al. 2013), spirals (Christiaens et al. 2014), and a warped velocity field, consistent with fast radial inflow (Rosenfeld et al. 2014), in the transitional disk HD 142527, as well as an inner clearing in the transitional disk Ophiuchus IRS 48 (Bruderer et al. 2014).

ALMA will also allow for the study of winds and outflows from disks, probing more tenuous and smaller-scale regions than ever before; a helical disk wind has already been detected around the HD 163296 gas disk (Klaassen et al. 2013).

The work presented here was inspired by an observational puzzle derived from IR observations. For all moderate- or high-inclination disks, the Keplerian motion of the gas molecules is expected to produce double-peaked emission-line profiles for the rovibrational lines produced within a few AU of the central star. Surprisingly, however, observations have revealed that CO rovibrational emission lines from some moderate-inclination disks are strongly single-peaked (as defined by the so-called line profile parameter; Bast et al. 2011). As they also have a small spatial extent, these emission lines are inconsistent with any Keplerian disk models. Furthermore, spectro-astrometry reveals that the lines cannot be explained solely as emission from an azimuthally symmetric Keplerian disk (Pontoppidan et al. 2011). As a group, the disks with strongly single-peaked emission lines also tend to have high rovibrational CO line/continuum ratios and signatures of high accretion rates (Bast et al.), including high UV fluxes (Yang et al. 2012) and high optical and IR veiling (e.g., Gahm et al. 2008; Salyk et al. 2008). In addition, several disks with single-peaked emission lines are known to have jets or outflows (Alencar et al. 2001; Wang et al. 2004; Herczeg et al. 2005). Strongly single-peaked profiles are seen in perhaps $\sim 30\%$ of CO rovibrational line-emitting disks (Bast et al. 2011), but recent results suggest that nearly all protoplanetary disks produce emission lines that are more single-peaked than expected for a Keplerian disk, and that they tend to have a slight blue asymmetry (Brown et al. 2013). Therefore, whatever phenomenon explains these observations may be widespread.

A possible explanation for these surprising observations was suggested by Pontoppidan et al. (2011), who showed that disk + disk wind models could reproduce the observed

line shapes, spectro-astrometric line profiles, and small spatial extent. However, while the models used by Pontoppidan et al. were originally derived from magnetohydrodynamic (MHD) wind simulations (Kurosawa et al. 2006), they were largely parameterized, and only loosely constrained by the available data. Yet, if the disk wind models used by Pontoppidan et al. are correct, disks may be losing mass at a rate of $\sim 1\%$ of their mass accretion rate, and the results of Brown et al. (2013) suggest that disk winds may in fact be universal. How might these winds affect disk evolution, or the formation of planets? The answers to these questions are essentially unknown and require that we gain a better understanding of the properties and driving mechanisms of these winds. If the disk wind cools quickly as it extends outward and its density drops, a low-critical-density, low-excitation tracer like ^{12}CO $J = 2-1$ may be a good choice for detecting a wind on larger scales and for studying its structure and kinematics.

In this work, we present ALMA observations of CO $J = 2-1$ from a prototypical source displaying evidence for a possible disk wind. The target of our study—the T Tauri star AS 205 N—shows strongly centrally peaked IR molecular emission lines with high line/continuum ratios (Salyk et al. 2008; Pontoppidan et al. 2011), a high and possibly highly variable accretion rate (Eisner et al. 2005; Salyk et al. 2013), and some evidence for an outflow (Mundt 1984). AS 205 N is also the northern and more massive component of a $1''.3$ (projected separation) binary system, in which the secondary star (AS 205 S) is itself a double-lined spectroscopic binary (Eisner et al. 2005). AS 205 is located at the northern edge of the Ophiuchus star-forming region, at a distance of ~ 125 pc (Mamajek 2008; Loinard et al. 2008).

In Section 2 we briefly describe the data acquisition and reduction. In Section 3 we present detections of ^{12}CO , ^{13}CO , and C^{18}O from the disks in the AS 205 binary system and discuss interesting features in the images and velocity fields. Then, in Section 4 we discuss possible explanations for these features, including an extensive discussion of their possible connection to the disk winds proposed to explain AS 205 N’s unusual IR spectroscopic features. Finally, we include a brief discussion of implications (Section 5) and conclusions (Section 6).

2. OBSERVATIONS AND REDUCTION

Observations of AS 205 N and S were obtained on UT 2012 March 27 and May 4, with the Cycle 0 extended configuration. The nearby quasar J1625–254, at a distance of 7.6 , was observed at ~ 11 minute intervals to correct for atmospheric variations. Short-term phase variations were corrected using the onboard water vapor radiometers. Fifteen 12 m antennas were available for both sets of observations, although one to two antennas were flagged at any given time during the observations. On March 27, the minimum and maximum baselines were 43 and 402 m (corresponding to minimum and maximum spatial scales of $\sim 0''.7$ and $4''$, 88 and 500 AU at 125 pc), respectively, and on May 4, they were 21 and 402 m (with a maximum spatial scale of $\sim 8'' = 1000$ AU). The total on-source integration time for each set of observations was 15.8 minutes, for a total integration time of 31.6 minutes.

Observations were obtained in four spectral windows of width 117 MHz, with a channel width of 30.5 kHz (0.04 km s^{-1}), corresponding to a spectral resolution of 61 kHz (0.08 km s^{-1}). Three of the spectral windows were centered at the frequencies of ^{13}CO 2–1 (220.399 GHz), ^{12}CO 2–1 (230.538 GHz), and

C^{18}O 2–1 (219.56 GHz). The fourth window was centered on an undetected CH_3OH transition (232.415 GHz) and was used for continuum measurement.

The data were reduced according to a standard procedure, using the Common Astronomy Software Applications (CASA) package (McMullin et al. 2007). Reduction steps included passband calibration, correction for atmospheric variations, and absolute flux calibration. Absolute flux was calibrated using observations and models of Titan. The calibrated measurement sets were then combined for the two dates. The continuum window was binned to a single channel and then CLEANed using the Clark algorithm and Briggs weighting with a robustness parameter of 0.5. The spectral windows were first continuum-subtracted and then binned to a channel spacing equal to the spectral resolution (0.08 km s^{-1}) and CLEANed in the same manner as the continuum window. Continuum subtraction was performed using a fit to the 232 and 219 GHz windows and either a constant model (for ^{12}CO) or a linear model (for ^{13}CO and C^{18}O). Inspection of line-free channels suggests continuum-subtraction residuals in the ^{12}CO maps of up to $\sim 10\%$ near the centers of AS 205 N and S; no significant residuals remain in the ^{13}CO and C^{18}O maps.

3. RESULTS

3.1. Basic Results

In Figure 1 we show the observed (CLEANed) ^{12}CO 2–1, ^{13}CO 2–1, and C^{18}O 2–1 zeroth-moment maps and 1.3 mm continuum images of the AS 205 system. Note the different gray scales and contour intervals for each row. Based on the continuum measurements, the separation of the two disks is $1''.3$, and the position angle of the binary is 214° . Previous works have found separations of $1''.3$ – $1''.4$ and position angles between 204° and 213° (Reipurth & Zinnecker 1993; Ghez et al. 1993; Koresko 2002; Prato et al. 2003; Eisner et al. 2005), with no coherent temporal evolution. Both sources appear to be detected in all three lines and in the continuum, and basic statistics for these detections are listed in Table 1.

For all maps, the synthesized beam is approximately $\sim 0''.7 \times 0''.5$ with a position angle of $\sim 90^\circ$ – 100° . The continuum emission appears unresolved or barely resolved, with a spatial FWHM ranging from $0''.63$ to $0''.76$ and a position angle of 99° —consistent with that of the synthesized beam. The line emission is spatially extended in all three isotopologues and for both components of the system, although the spatial extent of the northern component is larger than for the southern component. The ^{12}CO emission and ^{13}CO emission from the northern component appear asymmetric, with a larger spatial extent toward the north and northwest.

Although all isotopologues are present in the zeroth-moment maps near AS 205 S and AS 205 N, the ^{13}CO emission spatially associated with AS 205 S is actually dominated by gas at a similar velocity to AS 205 N. Therefore, some of this emission may instead be associated with AS 205 N. We also note that the C^{18}O emission near AS 205 S is detected in the zeroth-moment map only, and at only the 3σ level. Therefore, we caution that this detection is tentative and could, for example, arise from errors in continuum subtraction.

Channel maps and first-moment (velocity field) maps for the northern component in ^{12}CO and ^{13}CO are shown in Figures 2 and 3. Channel maps and first-moment maps for the southern component in ^{12}CO are shown in Figure 4. Line profiles for the three isotopologues are shown in Figure 5. ^{12}CO and ^{13}CO

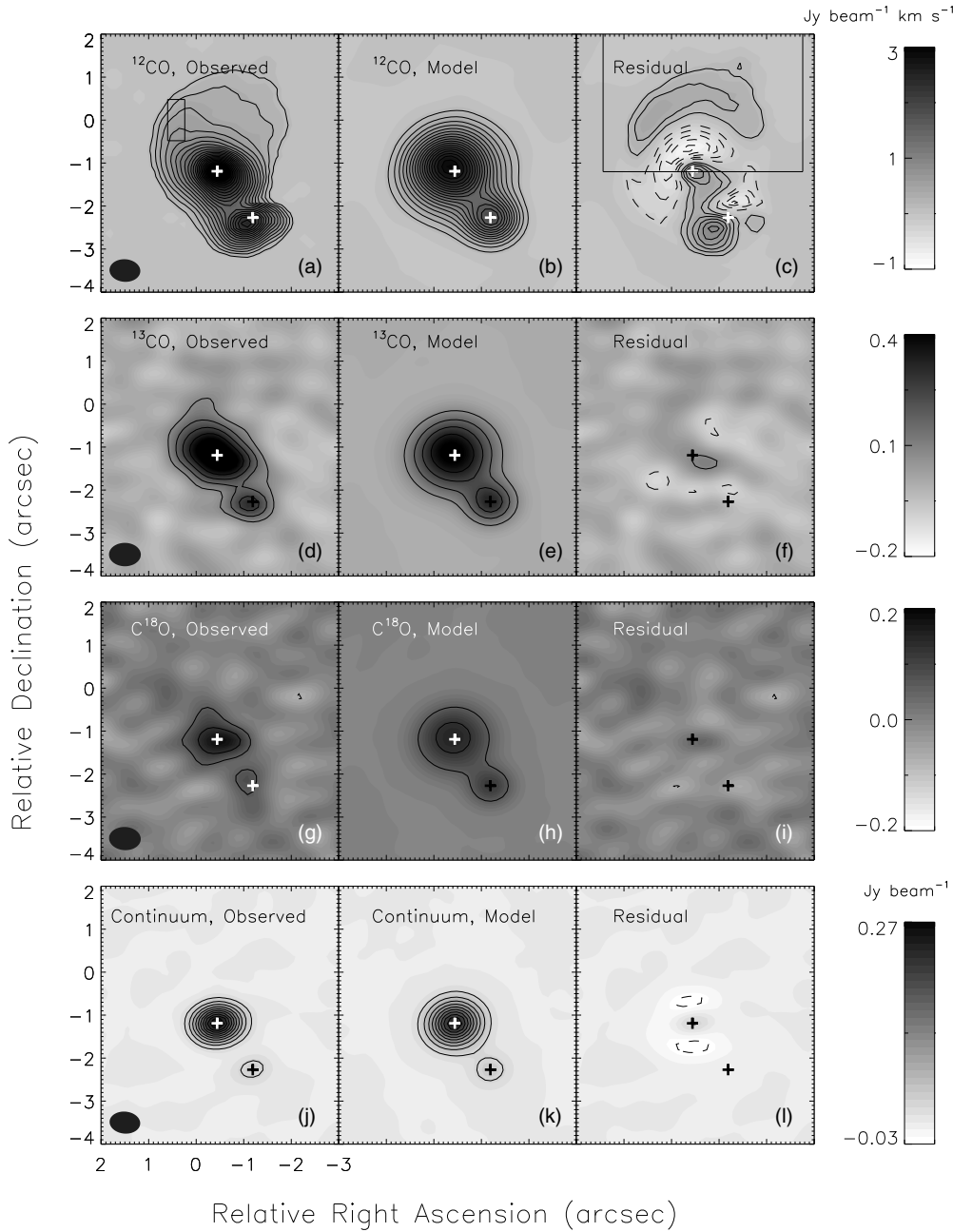


Figure 1. (a) Observed ^{12}CO 2–1 zeroth-moment (intensity) map. The box is used for calculations in Section 3.4.2. (b) Modeled ^{12}CO 2–1 zeroth-moment map. (c) ^{12}CO 2–1 model residuals. The box is used for calculations in Section 3.4.2. (d) Observed ^{13}CO 2–1 zeroth-moment map. (e) Modeled ^{13}CO 2–1 zeroth-moment map. (f) ^{13}CO 2–1 model residuals. (g) Observed C^{18}O 2–1 zeroth-moment map. (h) Modeled C^{18}O 2–1 zeroth-moment map. (i) C^{18}O 2–1 model residuals. (j) Observed continuum intensity. (k) Modeled continuum intensity. (l) Continuum model residuals. Note the different gray scales for each set of maps. For the ^{12}CO 2–1 and continuum observations, contours begin at 10σ and proceed in 10σ steps. For ^{13}CO and C^{18}O , contours begin at 3σ and proceed in 3σ steps. Dashed contours are negative. In all panels, the crosses mark the measured center of the continuum emission from AS 205 N and AS 205 S. The beam ellipse is shown in the bottom of the leftmost panels.

lines are computed for the entire system, including the northern and southern components and any extended emission, using a $6.^{\circ}48$ high by $4.^{\circ}32$ wide extraction box. The emission line for C^{18}O was computed for the northern component only, using a small $1.^{\circ}68$ high by $1.^{\circ}44$ wide extraction box, to reduce the contribution from the noisy background. The fluxes and line widths are summarized in Table 1. The ^{12}CO emission has a total flux (for both components combined) of $22.25 \text{ Jy km s}^{-1}$, consistent with the flux of $20.06 \pm 0.13 \text{ Jy km s}^{-1}$ found by Öberg et al. (2011) if we allow for a 15% error in absolute flux calibration.

Using the mean and standard deviation of the line centers, we estimate v_{LSR} of AS 205 N to be 4.29 ± 0.18 , consistent to within 1.6σ of the published stellar velocity of 1.97 ± 1.51 from Melo (2003), but inconsistent with the $-0.25 \pm 0.87 \text{ km s}^{-1}$ found by Eisner et al. (2005). The high and variable veiling in this source (Gahm et al. 2008) could contribute to large systematic errors in stellar velocities. For AS 205 S, we take the v_{LSR} for ^{12}CO ($0.80 \pm 0.09 \text{ km s}^{-1}$) to be the most likely value, since we were able to separate the signals from AS 205 N and AS 205 S (see Table 1). Eisner et al. (2005) find stellar velocities for the components of this spectroscopic binary of 11.05 ± 0.46 and

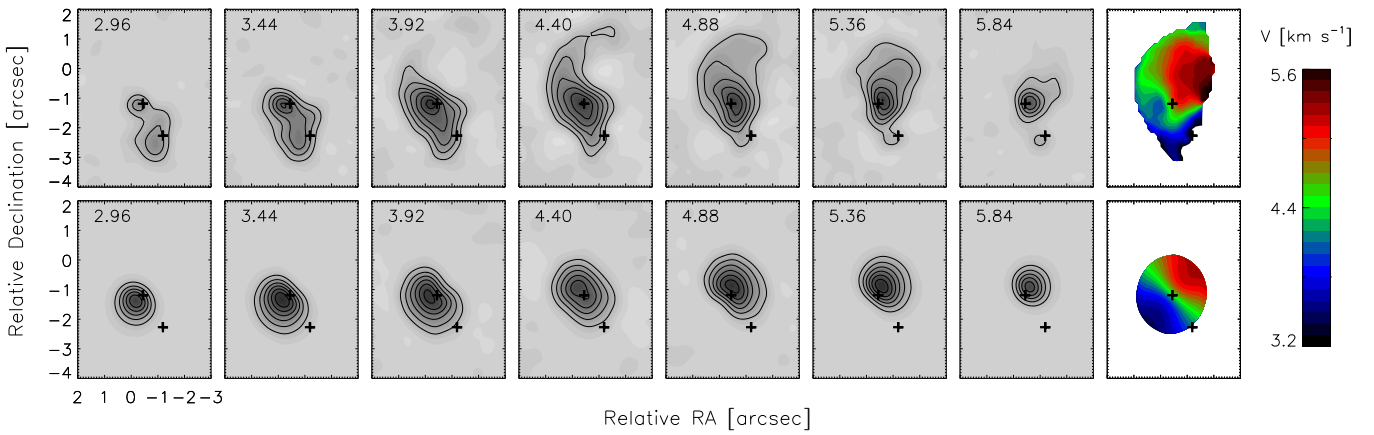


Figure 2. Channel maps of observed ^{12}CO emission (top) and a disk model (bottom), in addition to first-moment maps (right), for AS 205 N. Contours are multiples of 10σ . Labels in upper left show the central velocity (v_{LSR}) of the channel.

(A color version of this figure is available in the online journal.)

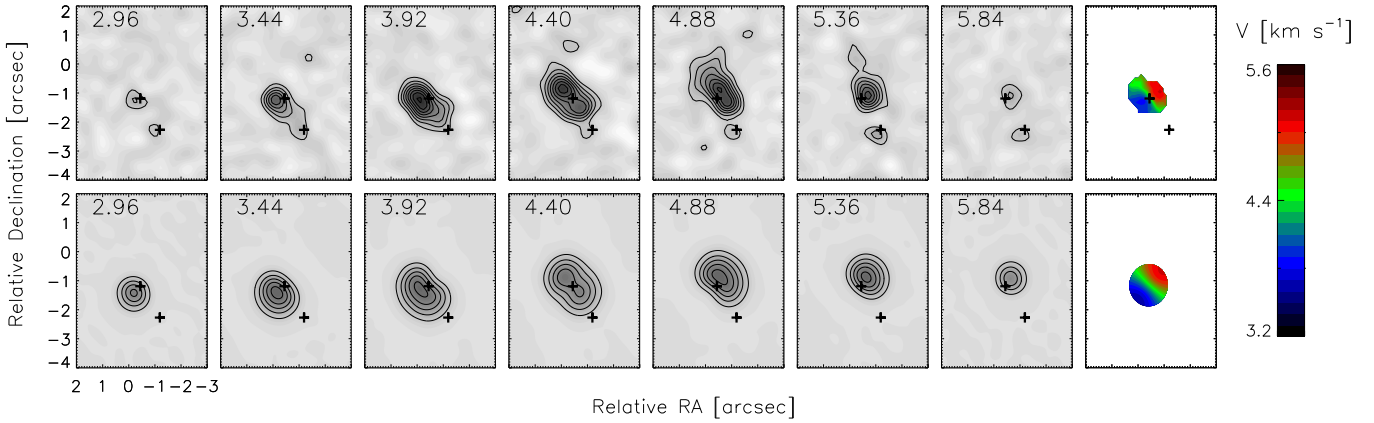


Figure 3. Channel maps of observed ^{13}CO emission (top) and a disk model (bottom), in addition to first-moment maps (right), for AS 205 N. Contours are multiples of 3σ .
(A color version of this figure is available in the online journal.)

Table 1
Detection Statistics and Line Parameters

Tracer	Flux (N, S) (Jy km s $^{-1}$)	FWHM (N, S) (km s $^{-1}$)	Line Center (N, S) (km s $^{-1}$)
$^{12}\text{CO}^{\text{b}}$	$19.23 \pm 0.27, 3.02 \pm 0.22$	$2.27 \pm 0.03, 2.59 \pm 0.18$	$4.48 \pm 0.01, 0.80 \pm 0.09$
$^{13}\text{CO}^{\text{c}}$	$1.86 \pm 0.04, 0.99 \pm 0.09$	$1.62 \pm 0.04, 2.68 \pm 0.24$	$4.45 \pm 0.02, 4.26 \pm 0.12$
C^{18}O	$0.34 \pm 0.03, 0.13 \pm -0.02$	1.62 ± 0.14	4.18 ± 0.07
Flux density (N, S) (mJy)		...	
Continuum	$377 \pm 2, 64 \pm 1$...	

Notes.

^a v_{LSR} .

^b It is not straightforward to separate the contributions from AS 205 N and S. For these calculations, we perform a Gaussian fit to the full ^{12}CO emission profile to determine the AS 205 N statistics. We then subtract the Gaussian fit from the line to obtain the emission line from AS 205 S.

^c Here we compute the statistics for AS 205 S by totaling the flux in the vicinity of AS 205 S. For ^{13}CO , the derived line center of $\sim 4 \text{ km s}^{-1}$ suggests significant contamination from AS 205 N.

$-6.36 \pm 1.11 \text{ km s}^{-1}$, with an average of $2.35 \pm 1.2 \text{ km s}^{-1}$, consistent with our result.

3.2. Disk Models

To aid with the analysis of the data, we constructed disk models to compare with the observed data. Dust radiative transfer was performed with RADMC (Dullemond & Dominik 2004),

and line radiative transfer with RADLite (Pontoppidan et al. 2009). Simulated ALMA data sets were created using the CASA routines *simanalyze* and *simobserve*. All simulated observations use the antenna configuration from the observations on 2012 May 4 and an exposure time of 30 minutes. Simulated data sets are shown in Figures 1–4.

Our nominal disk model for the northern component uses most of the same stellar and disk parameters derived by

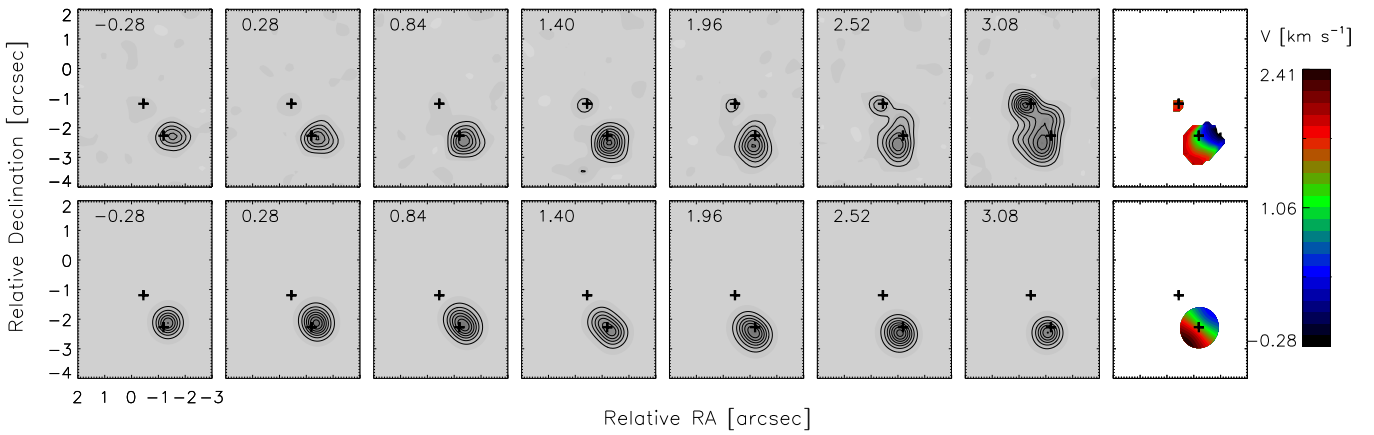


Figure 4. Channel maps of observed ^{12}CO emission (top) and a disk model (bottom), in addition to first-moment maps, for AS 205 S. Contours are multiples of 3σ . (A color version of this figure is available in the online journal.)

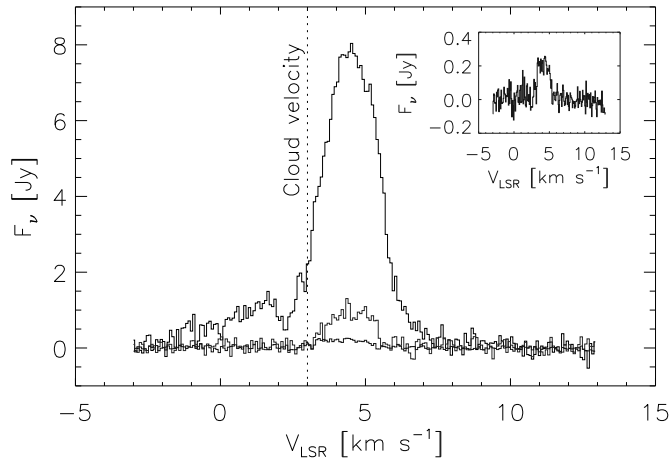


Figure 5. ^{12}CO (black), ^{13}CO (light gray), and C^{18}O (dark gray, and inset) emission-line profiles. ^{12}CO and ^{13}CO line profiles are derived from the whole system. The C^{18}O is from the northern component only, to reduce noise. Excess ^{12}CO emission at blue wavelengths is contributed by the southern component. The vertical dotted line marks the measured cloud velocity near AS 205.

Andrews et al. (2010) from a combined fit to the spectral energy distribution and millimeter visibilities— $R_\star = 3.7 R_\odot$, $M_\star = 1 M_\odot$, $T_\star = 4250 \text{ K}$, $R_{\text{in}} = 0.14 \text{ AU}$, $M_{\text{disk}} = 0.029 M_\odot$, and $H \sim 20 \text{ AU}$ at 80 AU , with $H/R \propto (R/80 \text{ AU})^{0.11}$. However, in contrast to Andrews et al. (2010), who use the similarity solution for surface density, Σ , we use a broken power law $\Sigma \propto (R/\text{AU})^{-0.9}$ out to $R_{\text{out}} = 80 \text{ AU}$, and $\propto (R/\text{AU})^{-12}$ beyond. We also use a simple grain opacity with 80% small amorphous astronomical silicates and 20% carbon grains. Less information is available in the literature for the southern component, and so for simplicity we utilize many of the same model parameters as for AS 205 N. However, we assume $R_\star = 4.2 R_\odot$, $M_\star = 0.6 M_\odot$, and $T_\star = 3450 \text{ K}$, values derived by Prato et al. (2003) but with a correction for the fact that the southern source is a spectroscopic binary (Eisner et al. 2005). We find a good match to the observed continuum data with a disk mass of $0.006 M_\odot$.

The CO 2–1 emission is dominated by disk regions with densities well above the critical density for this line (e.g., Bruderer et al. 2012), and even the more tenuous winds we are investigating here are predicted to have densities at or above the critical density out to large distances from the star (Panoglou et al. 2012). Therefore, all models assume local thermodynamic

equilibrium conditions. We assumed a gas-to-dust ratio of 100 and used a parameterized gas temperature increase in the disk atmosphere, following the procedure described in Zhang et al. (2013). In particular, we set $T_{\text{gas}} - T_{\text{dust}} = 300 \times e^{-r/30 \text{ AU}}$ above the $\tau = 1$ disk surface. We also assumed an H_2/CO ratio of 5000 (Lacy et al. 1994) and a CO freeze-out temperature of 17 K. For isotopologue abundances, we assumed $^{12}\text{CO}/^{13}\text{CO} = 60$ and $^{12}\text{CO}/\text{C}^{18}\text{O} = 500$. Since our limited information would result in strong model degeneracies were we to try to exactly match the observed data, we simply made small adjustments to the total flux produced by the models to approximately match the data. For AS 205 N, we multiplied the continuum models and the ^{12}CO , ^{13}CO , and C^{18}O continuum-subtracted models by factors of 1.3, 1.4, 0.4, and 0.2. For the southern source models, we multiplied by factors of 1, 1.2, 0.5, and 0.3. None of the conclusions in this work depend on the absolute flux of the models.

We find that an inclination of $\sim 15^\circ \pm 5^\circ$ is required to fit the observed ^{13}CO velocity field for AS 205 N. Previous spectro-astrometric results, which also resolved the binary, found a disk inclination of $\sim 20^\circ$. Using the ^{12}CO velocity field, we find a disk inclination of $25^\circ \pm 10^\circ$ for AS 205 S. These inclinations and error bars are determined via by-eye examination of the channel maps and residuals, and based on a combination of the relative fluxes in the low- and high-velocity channels, as well as the shapes of the maps. We also find that the disk around AS 205 S must be significantly smaller than AS 205 N, and we set $R_{\text{out}} = 35 \text{ AU}$. We discuss this result in more detail in Section 3.3. There is some uncertainty in the literature about the mass of AS 205 S. Eisner et al. (2005) derive a larger mass than assumed in our nominal model, $1.28 M_\odot$, along with temperatures for AS 205 N and S of 3800 and 4000 K , respectively, and a total luminosity of $0.7 L_\odot$. With this alternative choice of parameters, we find an inclination for AS 205 S of $\sim 15^\circ$. Given the limited resolution of our observations compared with the size of the AS 205 S disk, spatial information cannot be used to break the degeneracy between stellar mass and inclination.

Figure 3 shows that the AS 205 N disk model deviates from the ^{13}CO data in some respects. In particular, the high-velocity emission is slightly overpredicted. However, decreasing the inclination of the model would produce maps less elongated than the data at low velocities. A similar discrepancy was noted by Rosenfeld et al. (2012) for TW Hya and attributed to a warp in the TW Hya disk. In our case, the discrepancy could instead

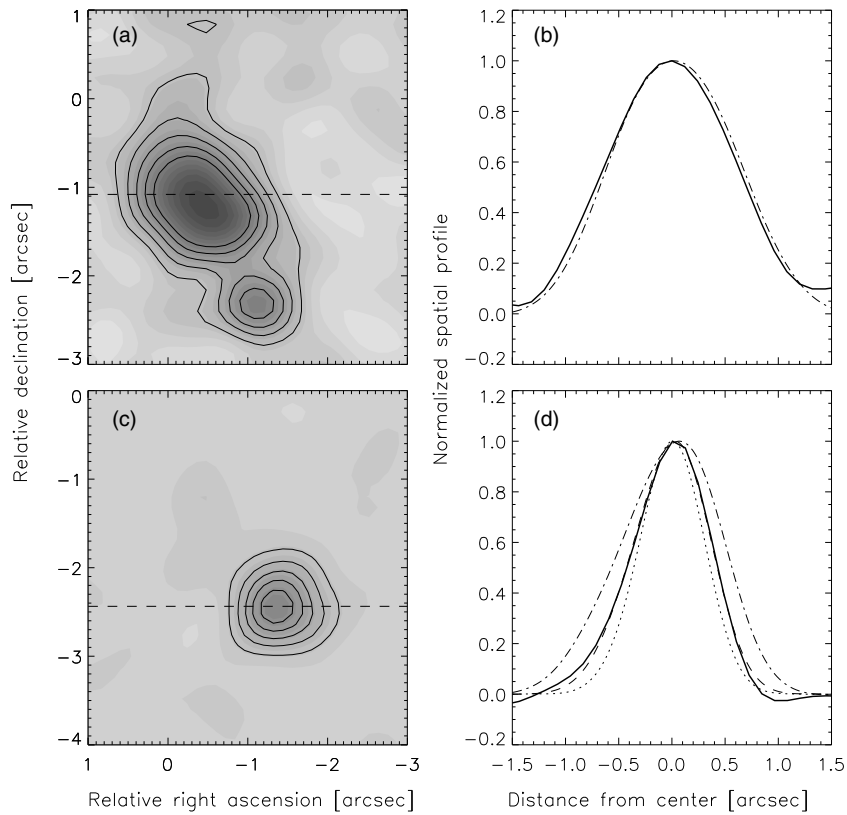


Figure 6. (a) Zeroth-moment map of ^{13}CO 2-1 emission from AS 205 N. The dashed line shows where the spatial profile is extracted. (b) The extracted spatial profile for AS 205 N derived from the data (solid line) and the nominal disk model with $R_{\text{out}} = 80$ AU (dot-dashed line). (c) Channel map of ^{12}CO emission from AS 205 S at $v = 0.84 \text{ km s}^{-1}$ (same as the third panel in the top half of Figure 4). The dashed line shows where the spatial profile is extracted. (d) Extracted spatial profiles for AS 205 S. The solid line shows the data, while the dot-dashed, dashed, and dotted lines show disk models with $R_{\text{out}} = 60$, 35, and 20 AU, respectively.

be related to the other evidence for non-Keplerian motions in our data set, which is discussed in much greater detail throughout this work.

The position angles of the AS 205 N and AS 205 S disks are observed to be $\sim 135^\circ \pm 5^\circ$ and $\sim 320^\circ \pm 10^\circ$, respectively, and are therefore misaligned by nearly 180° . The relative alignments of the disk rotation axes cannot be unambiguously determined unless the near and far sides of both disks are known. The disks are either oriented in the same direction with respect to the plane of the sky, with rotation vectors nearly anti-aligned, or are oriented in opposite directions with respect to the plane of the sky, with rotation vectors having a misalignment of $40^\circ(25^\circ + 15^\circ)$.

The ^{13}CO emission from AS 205 N shows a distinct NE/SW asymmetry, with NE regions being brighter. This is especially apparent in the 4.40 km s^{-1} channel in Figure 3, for example. If attributed solely to disk emission, this effect is naturally produced if the NE side is the far side of the disk, owing to a combination of projection and optical depth effects (e.g., Pontoppidan et al. 2009; Rosenfeld et al. 2013). This orientation is consistent with the spectro-astrometric results of Pontoppidan et al. (2011). However, this interpretation of the asymmetry is not definitive, as our data set includes several features that are not well explained by a disk model alone. It is not possible to determine the near/far-side orientation of the disk around AS 205 S with these data.

3.3. Truncation of Disk Around AS 205 S

In this work, our disk models assume a broken power-law surface density that declines sharply at some radius R_{out} . For AS 205 N, the data are consistent with $R_{\text{out}} \sim 80$ AU.

This is demonstrated in Figure 6, which shows a normalized spatial profile along a cut in the zeroth-moment map of ^{13}CO emission. We have chosen to extract an E-W oriented profile to minimize contamination from the extended emission observed toward the NW of the image, as well as from the southern source. The FWHM of the observed spatial profile is $\sim 1''.2$. We show that the observed ^{13}CO spatial profile is well reproduced by our nominal disk model.

The line emission from AS 205 S, however, is more compact. Because the zeroth-moment ^{12}CO map is dominated by emission from AS 205 N, we consider in this case a single channel map, shown in Figure 6, which does not suffer any contamination. In this case, the FWHM of the emission is only $0''.9$, and a model with $R_{\text{out}} = 80$ AU does not fit the data. Instead, we find that models with $R_{\text{out}} \sim 30$ – 40 AU provide a reasonable fit. In principle, the spatial extent of the image also depends on the disk inclination and position angle; however, we find the spatial extent of the model to be relatively insensitive to position angle and inclinations in the range of 15° – 35° .

This truncation can be compared with expectations from binary disk truncation models. For example, the parametric fit to truncated disk sizes from Pichardo et al. (2005) predicts a relative size ratio for the two disks of a binary that depends only on the binary mass ratio (assuming that the disks are close enough to each other to be truncated). For this system, with $M_1 = 1.0 M_\odot$ and $M_2 = 0.6 M_\odot$, the predicted ratio of disk sizes would be ~ 1.3 . Our best-fit disk models have ratios near two—slightly larger than predictions. With the masses assumed by Eisner et al. (2005), $M_1 = 1.2 M_\odot$ and $M_2 = 1.28 M_\odot$, the two disks would be expected to be nearly the same size, which is not consistent with our observations.

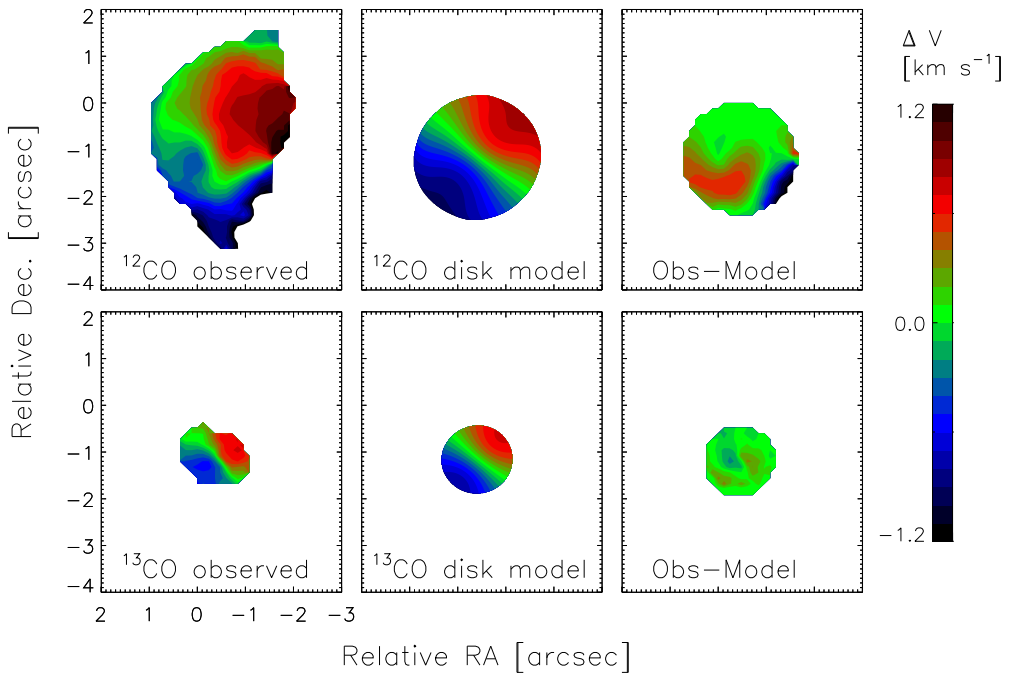


Figure 7. Comparison of observed and modeled ^{12}CO velocity fields (first-moment maps), with velocity relative to $v_{\text{LSR}} = 4.4 \text{ km s}^{-1}$.
 (A color version of this figure is available in the online journal.)

3.4. Asymmetric Emission and Velocity Fields

3.4.1. Basic Characteristics of Extended Emission

One of the most striking results of this work is the nonaxisymmetric excess emission stretching northeast of AS 205 N, seen at the 10σ – 20σ level in the ^{12}CO zeroth-moment map and channel maps (Figures 1(a) and 2) and at the 3σ level in the ^{13}CO zeroth-moment map (Figure 1(d)). The ^{12}CO emission, extending to distances of $\sim 2''$, is much wider than the synthesized beam width with major axis $\sim 0''.7$ and covers an angular extent of nearly 180° . Figure 2 also demonstrates that most of the extended emission consists of low-velocity gas—with $\sim 1.2 \text{ km s}^{-1}$ of the mean source velocity.

3.4.2. Mass and Optical Depth

Using the ^{12}CO model residuals, we can estimate the mass and optical depth of the spatially extended gas emission. Using the large box shown in Figure 1(c), we find a total flux of $1.0 \pm 0.2 \text{ Jy km s}^{-1}$. We have also computed the flux without including the negative values and have tested a range of possible scalings for the disk model (each producing different residuals). These tests imply that the systematic uncertainty in the total flux is a factor of a few. The temperature of the emission is essentially unknown. Assuming that the emission is optically thin and has a low excitation temperature of 30 K, we find a total ^{12}CO mass of $2 \times 10^{-9} M_\odot$, or a total H_2 mass of $1 \times 10^{-5} M_\odot$ assuming an H_2/CO ratio of 5000. For a much higher excitation temperature of 1000 K, the total mass would be about 20 times larger. We also compute flux and mass upper limits using the ^{13}CO residuals in this same box. We find a total flux of $< 0.6 \text{ Jy km s}^{-1}$ (a 3σ limit) and a corresponding mass of $< 2 \times 10^{-9} M_\odot$ of ^{13}CO , implying a $^{12}\text{CO}/^{13}\text{CO}$ ratio > 1 .

We can also evaluate the optical depth to determine whether τ reaches high values. For the small box in Figure 1(a), assuming that the observed flux is proportional to τ and taking a very conservative (i.e., narrow, to maximize τ) local line broadening

of 10 m s^{-1} , we compute a CO column density of $\sim 10^{-6} \text{ g cm}^{-2}$, corresponding to an optical depth of 0.9. Therefore, the emission may be optically thick, and we consider our mass estimate a lower limit. The $^{12}\text{CO}/^{13}\text{CO}$ ratio in this box is > 6 and therefore consistent with either optically thin or moderately optically thick emission, assuming that the true isotopic ratio is similar to the values of ~ 50 – 150 found in nearby clouds or the interstellar medium (Goto et al. 2003).

3.4.3. Gas/Dust Ratio

Finally, we can estimate the gas/dust ratio of the extended emission, by comparing the line and continuum emission. In the large box defined in Figure 1(c), there is no detected dust emission above the noise level, which has an rms value of $\sim 2 \text{ mJy beam}^{-1}$. Assuming that the emission is optically thin, and taking an excitation temperature of 30 K and a grain opacity of $2 \text{ cm}^2 \text{ g}^{-1}$ (Beckwith et al. 1990), we find a 3σ limit to the dust mass of $< 5 \times 10^{-5} M_\odot$. Utilizing the gas mass from above, we find that the gas/dust ratio is $\gtrsim 0.4$. Thus, the constraint on the gas/dust ratio of the extended emission is weak, with both subcanonical (< 100) and supercanonical (> 100) values permitted by the data.

3.4.4. Non-Keplerian Velocity Field

The ^{12}CO and ^{13}CO first-moment maps also show a distinct “S”-shaped warp in the velocity field, which is different from expectations for a Keplerian disk. Figure 7 shows deviations of the observed velocity fields from our nominal disk model. The observations deviate from expectation by as much as $\sim 1 \text{ km s}^{-1}$.

4. WHAT IS THE ORIGIN OF THE EXTENDED EMISSION AND NON-KEPLERIAN VELOCITY FIELD?

We have identified low-velocity, wide-angle, spatially extended ^{12}CO emission from AS 205 N, as well as non-Keplerian ^{12}CO and ^{13}CO velocity fields. Here we discuss possible physical explanations for this extended and asymmetric emission.

4.1. Molecular Cloud Emission

One possible explanation for our observations is that we are seeing small-scale structure in the surrounding molecular cloud, whose emission is primarily resolved out by the interferometer owing to its large spatial scale. The Ophiuchus cloud region was mapped in ^{12}CO 1–0 by de Geus et al. (1990). AS 205 N lies to the north of most of the prominent filaments in the region and so is less likely to suffer from cloud contamination than regions closer to the core of Ophiuchus. More importantly, the local cloud velocity is $\sim 3 \text{ km s}^{-1}$, and, as shown in Figure 5, this velocity is far from the observed emission-line center. Additionally, much of the spatially extended emission we observe is redder than the emission-line center, further separating it from the cloud velocity. Velocities $\gtrsim 4.5 \text{ km s}^{-1}$ are only observed in the ^{12}CO 1–0 cloud maps at large distances ($\gtrsim 5^\circ$) from AS 205 N. Therefore, we do not believe that molecular cloud emission can be the cause of the observed spatially extended emission.

4.2. Envelope

Based on a variety of evolutionary indicators, AS 205 N is a Stage II source, with a disk but no envelope. According to the classification scheme of Greene et al. (1994), Class II objects (believed to represent Stage II) have 2–24 μm spectral indices, $\alpha = (d \log \lambda S_\lambda / d \log \lambda)$, between -1.6 and -0.3 , while AS 205 N has a 2–24 μm spectral index in the range of -1 to -0.4 . AS 205 N also has a bolometric temperature between 1200 and 1400 K⁶, while Class II objects are defined to have $T_{\text{bol}} > 650 \text{ K}$ (Chen et al. 1995). Furthermore, AS 205 has no detectable envelope in the millimeter maps obtained by Andre & Montmerle (1994) (with a beam size of $12''$), while all of the Class 0/I objects in their sample do show resolved envelope emission. In addition, the total 1.3 mm single-dish flux density of $450 \pm 90 \text{ mJy beam}^{-1}$ (assuming a 20% flux uncertainty; Andre & Montmerle 1994) is consistent with our measured system flux density of 441 mJy, suggesting little to no unseen envelope material. Attributing the 9 mJy difference to an envelope (assuming $T = 30 \text{ K}$ and $\kappa = 0.02 \text{ cm}^2 \text{ g}^{-1}$, which assumes a gas/dust ratio of 100) would imply a mass of $0.001 M_\odot$ —at least an order of magnitude lower than typical envelope masses in Ophiuchus (Andre & Montmerle 1994), although the large error bars on the single-dish measurement could allow a mass up to $0.01 M_\odot$. Therefore, AS 205 sits in the Class II regime, although the presence of a very low mass envelope cannot be excluded.

However, these ALMA observations represent a new resolution regime for observations of low- J CO emission from protoplanetary disks, and studies at similar resolution have so far focused on more evolved transition disks (e.g., Andrews et al. 2012; Casassus et al. 2013). Instead, AS 205 N's somewhat high spectral index, as well as its relatively high accretion rate ($7 \times 10^{-7} M_\odot \text{ yr}^{-1}$; Eisner et al. 2005) and disk mass, could imply that it sits at the evolutionarily younger end of Stage II. Therefore, in principle this extended emission could represent the first observation of a small-scale, low-mass remnant of the natal envelope. However, this hypothesis suffers from stability arguments. Cloud material at a distance of $2''$ should not be stable in a system with a $1''.3$ binary; this distance is too far

to be stable circumprimary material and too close to be stable circumbinary material (Artymowicz & Lubow 1994).

4.3. Accretion from a Circumbinary Disk

We consider here whether the observations might be explained as accretion flows from a circumbinary disk. The arc-like structures seen in the extended ^{12}CO emission near AS 205 N appear similar to those observed around other $\sim 1''$ separation binaries, such as UY Aur, GG Tau, and SR 24 (Duvert et al. 1998; Close et al. 1998; Roddier et al. 1996), structures that are posited to represent accretion streamers from circumbinary disks. Since this scenario requires the existence of a circumbinary disk, we discuss its possible existence below.

Based on the nondetection of a circumbinary ring in ^{12}CO emission, AS 205 cannot have a circumbinary disk similar to those around either GG Tau or UY Aur. GG Tau has a circumbinary disk extending from $\sim 1''$ to $2''$ from a $0''.24$ binary (White & Ghez 2001), with a total mass of $\sim 0.1 M_\odot$ (Piétu et al. 2011). The UY Aur circumbinary disk has a radius of $\sim 500 \text{ AU}$ and a mass of $\sim 10^{-3} - 10^{-2} M_\odot$ (Duvert et al. 1998). Assuming a face-on circumbinary ring extending from $2''$ to $6''$ (250–750 AU), an excitation temperature of 30 K, an $\text{H}_2:\text{CO}$ ratio of 5000, and using a 3σ upper limit derived from our zeroth-moment ^{12}CO map ($0.03 \text{ Jy km s}^{-1} \text{ beam}^{-1}$), we derive an upper limit to the mass of a circumbinary disk around AS 205 of $10^{-4} M_\odot$ —significantly lower in mass than that observed around either GG Tau or UY Aur. Note that we use a CO abundance consistent with the ^{13}CO abundance utilized by Duvert et al. (1998), and so the choice of CO abundance does not affect the comparison between the two disks. In addition, we note that our observations are sufficiently sensitive to detect disks with similar surface densities as those observed around GG Tau or UY Aur.

The circumbinary disk could potentially remain hidden if it were significantly more extended (and therefore resolved out by the interferometer). We are sensitive to circumbinary structure up to $\sim 8''$. Since the observed ^{12}CO emission extends no more than $\sim 2''$, it cannot represent an accretion streamer from an $8''$ wide disk. Models of this process (e.g., Günther & Kley 2002; Ochi et al. 2005; Hanawa et al. 2010) show continuity of the accretion streamers out to the inner edge of the circumbinary disk.

It is also possible that significant freeze-out of CO could hide a circumbinary disk from our view. However, single-dish flux measurements for this source place upper limits on the total mass of the system. AS 205 has a single-dish 1.3 mm flux consistent with its interferometric flux (as discussed in Section 4.2) and therefore consistent with little or no unseen material. Nevertheless, the large error bars on the absolute value of the 1.3 mm flux could allow for a mass of up to $\sim 0.01 M_\odot$ (where this implicitly assumes a gas/dust ratio of 100). We note that this situation is in contrast to the binary SR 24, which shows features in scattered light that have been attributed to accretion streamers (Mayama et al. 2010) and, therefore, could be considered an analog to AS 205. SR 24 has a single-dish flux three to four times higher than its interferometric flux (Andrews & Williams 2005), consistent with a significant amount of extended emission—a mass of $\sim 0.02 - 0.03 M_\odot$, assuming $\kappa_{1.3 \text{ mm}} = 0.02 \text{ cm}^2 \text{ g}^{-1}$ and $T = 30 \text{ K}$.

In conclusion, we show that observations of AS 205 place very firm limits on the possible mass of a CO-rich disk ($\lesssim 10^{-4} M_\odot$), and the single-dish flux is consistent with no unseen dust, although a total disk mass of up to $0.01 M_\odot$ (assuming a

⁶ The exact numbers for the spectral index and bolometric temperature depend on whether or not binary-unresolved photometry is included in the calculation. Photometry is from Eisner et al. (2005), Liu et al. (1996), Prato et al. (2003), McCabe et al. (2006), and Andrews & Williams (2007a, 2007b).

gas/dust ratio of 100) is allowed by the large error in absolute flux. With no evidence of a large reservoir to supply mass to the circumstellar disks, we believe that it is unlikely that we are observing accretion streams from a circumbinary disk. Additional single-dish measurements would be helpful to place firmer limits on any possible unseen material in this system.

4.4. Tidal Stripping by AS 205 S

Another possible explanation for our observations is tidal stripping by AS 205 S. This explanation has been previously invoked by Cabrit et al. (2006) to explain the morphological and kinematic signatures in the disk around the T Tauri star RW Auriga A, which bears some interesting similarities to our observations. RW Aur is a 1''.4 binary whose ^{12}CO 2–1 emission shows a redshifted “tail”-like feature extending to 2'', although at somewhat higher velocities, up to $\sim 7 \text{ km s}^{-1}$ —equivalent to $2\text{--}2.5 \text{ km s}^{-1}$ if adjusted to the 15° inclination of AS 205 N.

We first evaluate the relevance of tidal effects by computing the tidal radius of the secondary. For $M_1 = 1.0 M_\odot$ and $M_2 = 0.6 M_\odot$, the binary mass ratio is $\mu = M_2/(M_1+M_2) \approx 0.38$. The corresponding Lagrangian point L_1 (Murray & Dermott 1999) is located at $\sim 0.55 r_{\text{sep}} \sim 89 \text{ AU}$ from M_1 , that is, reaching just outside the $\sim 80 \text{ AU}$ outer radius of the AS 205 N disk. Consequently, some perturbations to the disk symmetry are to be expected.

Tidal effects will be strongest if the encounter is resonant or “quasi-resonant” (D’Onghia et al. 2010). Roughly speaking, as in a forced oscillator model, tidal interactions are most pronounced when there is frequency matching between the internal modes of the victim (in this case, the disk around AS 205 N) and the external forcing frequency exerted by the perturber, M_2 . In other words, maximum response occurs at the disk radii R such that the internal orbital frequency $\Omega(R) = \sqrt{GM_1/R^3}$ is an integer fraction of $\Omega_{\text{orb}} = \sqrt{G(M_1 + M_2)/p^3}$, where p is the pericenter distance.⁷ Note that the resonance also requires a prograde orbit of the perturber with respect to the victim’s spin.

A single passage by the perturber can excite prominent two-armed spirals (similar in morphology to what we observe) in the victim provided that the resonance occurs within the victim’s disk’s radial extent (see, e.g., Barnes & Hernquist 1996; Mihos & Hernquist 1996; D’Onghia et al. 2010). However, if the pericenter distance, p , is equal to the binary projected separation of $\sim 160 \text{ AU}$ or larger, low-order near-resonance is not achieved for radii inside the primary’s disk with our assumed $\mu = 0.38$. To achieve low-order resonance, AS 205 S would need to be more massive. As discussed in Section 3.2, there is some uncertainty about the mass of AS 205 S. With the AS 205 S mass estimate derived by Eisner et al. (2005), $\sim 1.3 M_\odot$, resonant forcing would occur at $\sim 70 \text{ AU}$, just inside the outer radius of the AS 205 N disk.

However, even if AS 205 S is massive enough to have low-order resonant interactions with the disk of AS 205 N, a major drawback of this explanation is that bound pairs are expected to be already devoid of gas at the lowest-order resonances that create strong two-armed features, since those resonances would be quickly cleared out after a few subsequent pericenter passages (Paczynski 1977; Artymowicz & Lubow 1994). Therefore, we

would need to be observing AS 205 during its first, or nearly first, encounter. This is unlikely if AS 205 is a bound pair, as the orbital period is approximately a few thousand years, while the estimated age of AS 205 is 10^5 yr (Prato et al. 2003).

It is also very unlikely that this is a first (flyby) encounter between two stars. Thies et al. (2005) suggest that close stellar encounters may be likely during the $\sim 6 \text{ Myr}$ lifetime of disks around stars in massive young clusters; with encounter probabilities of 10%–30% for encounter distances of 60–200 AU (assuming a cluster mass of $500 M_\odot$ and a size of 0.3 pc), one can expect ~ 100 close stellar encounters throughout the lifetime of the cluster. However, Ophiuchus is significantly less massive and dense than this model presumes, with a stellar mass of $\sim 53 M_\odot$ in the central 2 pc^2 of the ρ Oph cloud core (Kenyon et al. 1998), and, furthermore, AS 205 lies in a less dense region at the edge of the Ophiuchus cloud (de Geus et al. 1990). Assuming $53 M_\odot$ in 2 pc^2 , and using the equations found in Thies et al., we find encounter probabilities of a few $\times 10^{-5}$ out to 300 AU—equivalent to an expected number of collisions of a few $\times 10^{-3}$. Finally, we must compute not the likelihood of an encounter, but the likelihood of observing an encounter in progress. If we assume an encounter velocity of 1 km s^{-1} and an impact parameter of 500 AU, the encounter lasts $\sim 2000 \text{ yr}$ —a factor of 500 shorter than the cluster age of at least 1 Myr (e.g., Wilking et al. 2005); therefore, the probability of viewing an encounter is 500 times lower than the probability of an encounter occurring. These factors combined suggest that the probability of observing a flyby encounter with an impact parameter of a few hundred AU in this region is $< 10^{-5}$.

Although lower-order resonances do not appear to explain the features we observe, in the long run, the evolution of circumprimary and circumbinary disks is dominated by higher-order, weaker resonances. As with the lower-order resonances, the resonant forcing and the internal damping of the disk reach a quasi-stationary state, in which the disk size is nearly in equilibrium. A balance is reached between the viscous and the tidal torques, eventually defining the truncation radius of both circumprimary and circumsecondary disks (Artymowicz & Lubow 1994). However, one subtlety in the analysis by Artymowicz & Lubow (1994) is that the equilibrium truncation radius is reached only after a viscous relaxation timescale that depends on the binary eccentricity, the final disk radius, the disk aspect ratio and the disk viscosity. Therefore, for very young systems, transient responses on the disks are still possible during every pericenter passage, especially for very eccentric binaries. Unfortunately, at this point we are not able to pursue this analysis further owing to the largely unconstrained orbital properties of this system and the uncertain mass of AS 205 S.

4.5. Winds

Our observations might also be explained by some form of wind. Thermal (photoevaporative) winds are unlikely to explain our observations, as the driving radiation for these flows tends to destroy molecules (e.g., Gorti & Hollenbach 2009). On the other hand, MHD disk winds, which are believed to be (at least partly) responsible for the larger-scale bipolar jets and outflows emanating from young stars (e.g., Ferreira et al. 2006; Pudritz et al. 2007; Ray et al. 2007, and references therein), can produce relatively low-velocity winds with a significant molecular content (Panoglou et al. 2012).

MHD disk winds have launching velocities that are similar to the sound speed (e.g., Kurosawa et al. 2006); therefore, tracers of the wind-launching region can have relatively low velocities.

⁷ Strictly speaking, we are looking for an inner Lindblad resonance to take place within R_{out} , where the resonance condition is given by $m(\Omega(R) - s\Omega_{\text{orb}}) \approx \pm\Omega(R)$, and thus the inner Lindblad resonance occurs at a radius $R_{\text{ILR}} = (1/m)^{2/3}(1-\mu)^{1/3} p$.

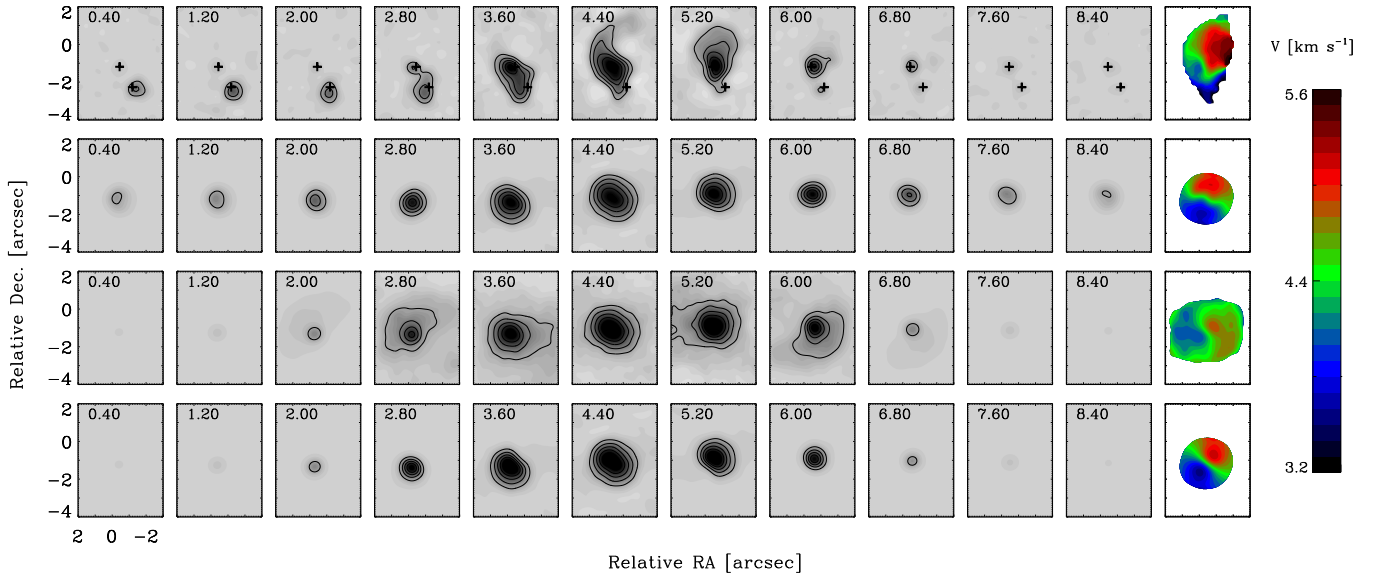


Figure 8. ^{12}CO channel maps and first-moment maps for, from top to bottom: observed data, our nominal disk+wind model, a disk+wind model with lower terminal velocity and higher mass-loss rate, and a disk-only model. Note the extended velocity coverage compared with Figure 2.

(A color version of this figure is available in the online journal.)

Temperatures in the launch region range from a few thousand K in the inner disk down to <100 K in the outer disk, with associated velocities in the range of $\sim 1\text{--}3 \text{ km s}^{-1}$. Observed launching velocities will be even lower if the streamlines are not directed toward the observer. However, poloidal velocities increase with distance along a streamline, reaching velocities as high as approximately a few hundred km s^{-1} in existing models (Pudritz et al. 2007), which are much higher than we observe here. Another obstacle for disk wind models may be whether there is sufficient overall gas density to explain the extended emission. In the models of Panoglou et al. (2012), CO densities of $\sim 0.1 \text{ cm}^{-3}$ result in a theoretical column density of $\sim 10^{-9} \text{ g cm}^{-2}$, assuming a column with vertical height 20 AU. This is three orders of magnitude below the observed lower limit to the column density, $\sim 10^{-6} \text{ g cm}^{-2}$. However, if lower terminal velocities are possible, then mass conservation will correspondingly increase the density in the wind, allowing models to match observations. We consider this in Section 4.5.2.

4.5.1. Relationship to Prior Observations of Outflows

The structure observed here is significantly different from the very collimated millimeter outflows observed around Class 0 and Class I disks (e.g., Jørgensen et al. 2007), many of which additionally appear to be tracing shocks on the inner surface of an outflow cavity in a surrounding envelope. However, Arce & Sargent (2006) imaged a sample of nine Class 0, I, and II young stellar objects in ^{12}CO 1–0 and noted that the millimeter emission becomes less collimated with evolutionary state. In fact, the emission we observe bears some resemblance to the structures observed by Arce & Sargent near the Class II sources T Tau and GK/GI Tau. The size scales of these structures are larger (up to $\sim 40''$ in length), but our observations are only sensitive to structures up to $\sim 8''$ in size. The velocities of these outflows are also higher than what we observe, typically $2\text{--}5 \text{ km s}^{-1}$ offset from the source velocity. In general, however, millimeter observations of Class II sources with outflows are limited, and even fewer observations have the spatial resolution of our observations, making comparisons difficult.

AS 205 N has some spectroscopic evidence for an active outflow. Although to our knowledge no optical jets have yet been imaged from this source, Mundt (1984) reported strong, narrow, blueshifted ($\sim 150 \text{ km s}^{-1}$) absorption features in Na D lines that are consistent with outflowing gas and observed in other sources with known outflows. In addition, Rigliaco et al. (2013) report a high-velocity component in observations of the $[\text{O I}] \lambda 6300$ line from AS 205 N, indicative of an outflow. It is also important to note that our observations were *motivated* by the suggestion of Pontoppidan et al. (2011) that a disk wind may explain observed single-peaked rovibrational CO emission lines, as well as asymmetric spectro-astrometric profiles of these same lines. In the next section we test whether the model utilized by Pontoppidan et al. can also explain our observations.

4.5.2. Comparison with Model Predictions

A simple parameterization of a disk wind was implemented by Pontoppidan et al. (2011) to fit observed rovibrational emission lines and incorporated into the radiative transfer code RADLITE (Pontoppidan et al. 2009). We describe this model and our choice of nominal model parameters in detail in the Appendix.

We find that the nominal wind model does not produce any appreciable extended emission, beyond that expected for a disk, owing to the low predicted densities at distances of hundreds of AU from the central star. However, the model does reproduce some of the other features of our observations. As shown in Figure 8, it produces additional flux at higher velocities compared with a disk-only model. The wind model also produces deviations from a Keplerian velocity field, including a curved first-moment map, demonstrated in Figure 9. The curvature in the model is due to two effects. At small radii, the dominant effect of the wind is that it makes the azimuthal velocities sub-Keplerian. At larger radii, the poloidal velocities are larger and begin to dominate the differences, causing the far side of the disk (in this case, toward the northeast) to be preferentially redshifted and the near side (toward the southwest) to be preferentially blueshifted. There are some similarities between the modeled and observed first-moment maps, in that both show a

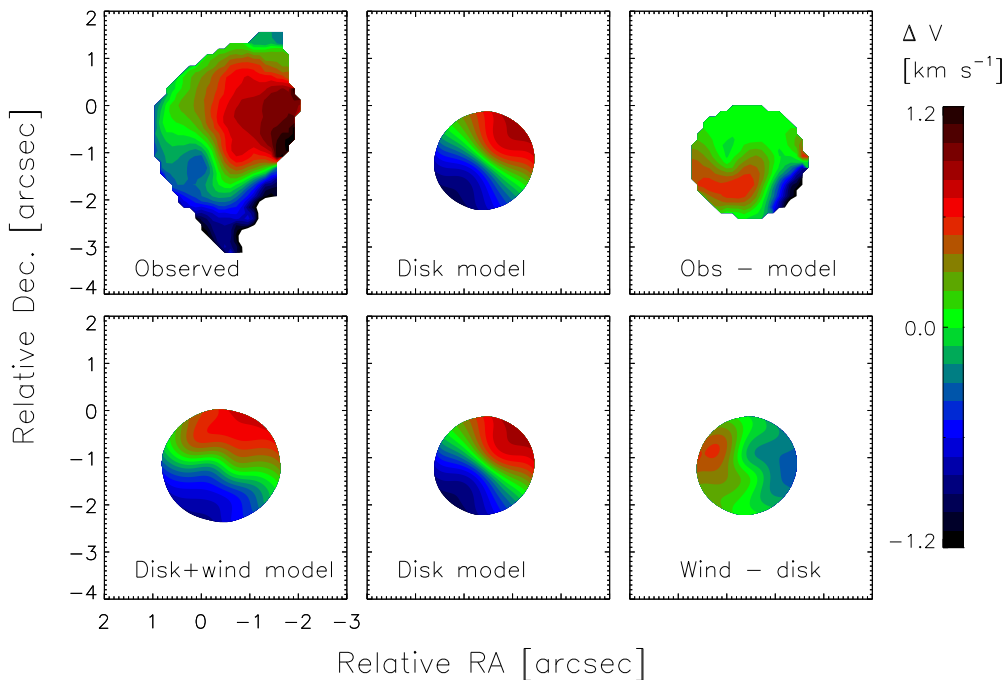


Figure 9. Top: observed and disk model ^{12}CO first-moment maps, relative to $v_{\text{LSR}} = 4.4 \text{ km s}^{-1}$, as well as their difference. Bottom: disk+wind and disk-only models, as well as their difference. All models assume that the far side of the disk is located toward the northeast.

(A color version of this figure is available in the online journal.)

complex “S”-like shape, although it is clear that the observed moment map is more complex than the modeled map.

A twisted velocity field can also arise from radial inflow, as suggested by Rosenfeld et al. (2014) to explain the velocity field of the transitional disk around HD 142527. Inflow and outflow can only be distinguished if the near and far sides of the disks are identified. In detail, HD 142527 is not an analog to AS 205 N; the fast radial inflow in HD 142527 is proposed to reconcile its high accretion rate and inner clearing, while AS 205 N has a full disk with no inner clearing. In addition, radial inflow alone would not explain the very extended ^{12}CO emission we observe. However, some wind models themselves predict that accretion may be dominated by restricted regions of the disk producing fast flows (Bai & Stone 2013). The resultant signature in the velocity field would then depend on the relative contributions of inflowing and outflowing gas to the observed emission and could vary throughout the disk, creating a complex velocity field. Unfortunately, disk-wide simulations of this process do not yet exist for comparison with observations.

Although the *nominal* wind model does not produce any appreciable extended emission, the density of the wind depends on the assumed mass-loss rate and terminal velocity. Figure 8 shows predicted channel maps for an alternative wind model, with a low terminal velocity (2 km s^{-1}) and high mass-loss rate ($2 \times 10^{-7} M_{\odot} \text{ yr}^{-1}$), which shows appreciable extended emission. The detailed structure does not obviously match our observations. It should be noted, however, that dynamical timescales for the binary orbit and the wind are similar, and so AS 205 S should cause perturbations to the wind structure. Therefore, our observations may be explained by a *combination* of disk winds and binary interaction.

In conclusion, wind models are in some ways consistent with the observations of AS 205 N. In particular, models produce a curved first-moment map with some similarities to the observed ^{12}CO velocity field. However, existing wind

models do not readily produce significant extended emission. Extended emission instead requires that the models be modified to have lower terminal velocities and/or higher mass-loss rates. Although the geometry of the resulting emission does not precisely match our observations, the detailed features we observe cannot be produced by an axisymmetric model. They could, however, be produced by interactions between the wind and the stellar companion, AS 205 S.

5. DISCUSSION

5.1. Why Has This Extended Emission Not Been Observed Before?

These are the highest-resolution observations of rotational CO emission from AS 205 to date. AS 205 was observed in ^{12}CO 3–2 by Andrews et al. (2009) with a beam size of $2''.19 \times 1''.60$ and in ^{12}CO 2–1 by Öberg et al. (2011) with a beam size of $3''.1 \times 2''.0$. In both cases, the beam size was not sufficient even to resolve the binary. Since the extended structure we observe is only a few arcseconds in size, a resolution of $\sim 1''$ or better is required.

Only a few disks have been observed in molecular lines at a resolution of $\sim 1''$ or better to date, as pre-ALMA observations were limited to the brightest disks. Therefore, it is difficult to say whether the phenomenon we observe is a common or unusual feature for protoplanetary disks. Interestingly, molecular line imaging at or near this resolution often seems to reveal surprises—for example, an extended CO disk around TW Hya (Andrews et al. 2012), an asymmetric, perhaps tidally induced “arm” near RW Aur (Cabrit et al. 2006), and asymmetric spiral arms in the disk of AB Aur (Corder et al. 2005; Piétu et al. 2005). ALMA observations of a few disks have already revealed azimuthal asymmetries and non-Keplerian flows (Casassus et al. 2013; Christiaens et al. 2014; Rosenfeld et al. 2014), as well as

a helical disk wind (Klaassen et al. 2013). Therefore, it seems likely that the resolution and sensitivity afforded by ALMA will continue to reveal many new small-scale asymmetric structures.

If the extended structure we observe here is a common feature for protoplanetary disks, this could have implications for the interpretation of lower-resolution observations. For low-resolution observations, the observed CO flux could incorrectly be attributed solely to a disk. Although it is difficult to determine the precise contribution to the flux from the wind, the box shown in Figure 1(c) contributes 5% of the total observed ^{12}CO 2–1 line flux. Also, if the wind has a different temperature than the disk, interpretation of observations of multiple CO isotopologues could incorrectly determine the gas temperatures. Since gas temperatures are in turn used to determine gas masses (e.g., Panić et al. 2008), this could have important consequences for our understanding of the planet-forming capabilities of disks.

5.2. If We Are Observing Mass Loss, What Is the Estimated Mass-loss Rate?

If we are actually observing a wind, with some simple assumptions, we can estimate the mass-loss rate. For this calculation, we use the CO observed in the large box in Figure 1(c) (see Section 3.4.2) and multiply by four to account for all directions of the wind. We obtain $M_{\text{gas}} \sim 8 \times 10^{-5} M_{\odot}$ for an excitation temperature of 30 K, or $M_{\text{gas}} \sim 2 \times 10^{-3} M_{\odot}$ for 1000 K. The mass-loss rate is $\dot{M}_{\text{loss}} \approx M_{\text{gas}} v_{\text{gas}} / D_{\text{gas}}$, where v_{gas} and D_{gas} are the actual velocity and length of the outflow, respectively. Both D_{gas} and v_{gas} are different from the observed distance and velocity, where $D_{\text{obs}} = D_{\text{gas}} \sin \theta$, $v_{\text{obs}} = v_{\text{gas}} \cos \theta$, and θ is the angle between the outflow and the observer. Thus, $\dot{M}_{\text{loss}} \approx (M_{\text{gas}} v_{\text{obs}} \sin \theta / D_{\text{obs}} \cos \theta)$. Taking $D_{\text{obs}} \sim 300$ AU, $v_{\text{obs}} \sim 1 \text{ km s}^{-1}$ and assuming $\theta = 15^\circ$ (equal to the best-fit disk inclination), we find $\dot{M}_{\text{loss}} \sim 10^{-8} \text{--} 10^{-7} M_{\odot} \text{ yr}^{-1}$. A different assumption about the inclination of the flow can either raise (for $i > 15^\circ$) or lower (for $i < 15^\circ$) the mass-loss rate. The disk + wind models described in Section 4.5.2 also required a rate of $\sim 10^{-7} M_{\odot} \text{ yr}^{-1}$ to produce significant extended emission.

Using observations of CO rovibrational line shapes and spectro-astrometry along with disk+wind radiative transfer models, Pontoppidan et al. (2011) estimated a similar or slightly lower mass-loss rate for AS 205 N— $9 \times 10^{-9} M_{\odot} \text{ yr}^{-1}$. Both results therefore suggest that $\dot{M}_{\text{loss}} / \dot{M}_{\text{acc}} \sim 0.01 \text{--} 0.1$.

6. CONCLUSIONS

We have presented here one of the most sensitive and highest-resolution millimeter-wave studies of a nearby T Tauri binary system and its accompanying gas disks, a study that was enabled by the newly available ALMA facility. It is clear from these observations that AS 205 N does not solely consist of a Keplerian gas disk, with differences including extended asymmetric ^{12}CO emission and a non-Keplerian velocity field. Although we have examined here several possible scenarios to explain these observations, no single scenario is able to completely explain these features. Two of the most promising explanations include a low-velocity wind or tidal stripping by the companion, but potential models will need to be explored further and fine-tuned if they are to match the observations. It may also be that we are observing wind-driven mass loss, modified by tidal interactions with the secondary. Future ALMA observations of disks in close binary systems, as well as disks with IR spectroscopic

evidence for disk winds, or evidence for larger-scale outflows, will be helpful for distinguishing between the two possible explanations.

Aside from the observations presented here, it is known that AS 205 N has other somewhat unusual properties compared with typical T Tauri disks. However, it is *not* unique, as there appears to be an emerging subpopulation of disks sharing properties with AS 205 N, properties including high accretion rates and veiling, as well as strongly single-peaked IR emission line profiles (e.g., Gahm et al. 2008; Bast et al. 2011; Pontoppidan et al. 2011). The story that these disks have to tell us is still unclear, but we are excited about the prospects of continuing to explore their interesting properties, and we expect that the mysteries of their origin will soon be revealed.

We thank the staff at the North American ALMA Science Center, especially Scott Schnee, for their help with the data reduction. C.S. acknowledges helpful discussions with Ilaria Pascucci, Sean Andrews, and Katherine Rosenfeld. C.S. also acknowledges the financial support of the NOAO Leo Goldberg Fellowship program. D.M. acknowledges helpful discussions with Dong Lai and Robert Harris. This paper makes use of the following ALMA data: ADS/JAO.ALMA#2011.0.00531.S. ALMA is a partnership of ESO (representing its member states), NSF (USA), and NINS (Japan), together with NRC (Canada) and NSC and ASIAA (Taiwan), in cooperation with the Republic of Chile. The Joint ALMA Observatory is operated by ESO, AUI/NRAO, and NAOJ. The National Radio Astronomy Observatory is a facility of the National Science Foundation operated under cooperative agreement by Associated Universities, Inc.

APPENDIX

RADLITE IMPLEMENTATION OF WIND MODEL

The wind model used in this work is based on the split-monopole parameterization described by Kurosawa et al. (2006) and originally from Knigge et al. (1995), in which the poloidal velocities follow a β -velocity law, the toroidal velocities conserve angular momentum, and the density is determined via mass conservation. The equations for velocity and density as a function of cylindrical radius, w , and distance along the streamline, l , are given in Kurosawa et al. (2006). The geometry of this model is completely defined by the (virtual) launching point, which is located a distance, d , below the star, and inner and outer radial extents, w_{wi} and w_{wo} . This parameterized model is meant to approximate magnetocentrifugal wind models, originally suggested by Blandford & Payne (1982) and Pudritz & Norman (1983).

The wind model was implemented into the line radiative transfer code RADLite by Pontoppidan et al. (2011). RADLite takes as input an arbitrary density, velocity, and temperature grid. In this implementation the densities and velocities above some defined surface level, τ_{surf} , are simply replaced by the equations found in Kurosawa et al. (2006). τ_{surf} is a vertical optical depth computed at $0.55 \mu\text{m}$. The temperatures, and the densities below τ_{surf} , take whatever form the user may choose; in our case, they are described by the disk model discussed in Section 3.2. Parameters used in our nominal model are similar to those used by Pontoppidan et al. and are listed in Table 2. Short definitions of the parameters are provided; detailed information about these parameters can be found in Kurosawa et al. (2006).

We also note a few clarifications. In our implementation, we replace the product $v_{\text{esc}} \times f$, the product of the local escape

Table 2
Disk Wind Parameters

Parameter	Value	Notes
d	$18.5 R_{\odot}$	1
β	2	2
v_{term}	20 km s^{-1}	3
\dot{M}_{wind}	$1.5 \times 10^{-9} M_{\odot} \text{ yr}^{-1}$	4
\dot{m}_{wind}	$2.8 \times 10^{-9} \text{ g cm}^{-2} \text{ s}^{-1}$	5
p	-7/2	6
R_s	19 AU	7
r_{surf}	0.75	8
w_{wi}	0.14 AU	9
w_{wo}	1 AU	10

Notes.

- 1 Distance between the star and the wind locus point, equivalent to $5 R_{\star}$ for AS 205 N, where $R_{\star} = 3.7 R_{\odot}$.
- 2 Wind acceleration parameter.
- 3 Wind terminal velocity.
- 4 Total wind mass-loss rate.
- 5 Mass-loss rate per unit area, at the innermost wind launching radius.
- 6 Power-law exponent for radial dependence of mass-loss rate.
- 7 Wind scale length.
- 8 τ at $0.55 \mu\text{m}$ taken as the launching height of the wind.
- 9 Cylindrical radius of the innermost wind launching radius, here taken to be the inner edge of the disk.
- 10 Cylindrical radius of the outermost wind launching radius.

velocity and the ratio of the terminal velocity to the escape velocity, with a single parameter, v_{term} , representing the terminal velocity of the wind. Although v_{esc} varies with radius, in practice the small launching region of the wind precludes a large range in v_{esc} , so this substitution is a useful conceptual simplification. In addition, we provide the total mass-loss rate (\dot{M}), integrated over the disk surface participating in the wind, although we also include the mass-loss rate per unit area at the innermost launching point (\dot{m}) defined in Kurosawa et al. (2006).

REFERENCES

- Alencar, S. H. P., Johns-Krull, C. M., & Basri, G. 2001, *AJ*, **122**, 3335
 Andre, P., & Montmerle, T. 1994, *ApJ*, **420**, 837
 Andrews, S. M., & Williams, J. P. 2005, *ApJL*, **619**, L175
 Andrews, S. M., & Williams, J. P. 2007a, *ApJ*, **659**, 705
 Andrews, S. M., & Williams, J. P. 2007b, *ApJ*, **671**, 1800
 Andrews, S. M., Wilner, D. J., Hughes, A. M., Qi, C., & Dullemond, C. P. 2009, *ApJ*, **700**, 1502
 Andrews, S. M., Wilner, D. J., Hughes, A. M., Qi, C., & Dullemond, C. P. 2010, *ApJ*, **723**, 1241
 Andrews, S. M., Wilner, D. J., Hughes, A. M., et al. 2012, *ApJ*, **744**, 162
 Arce, H. G., & Sargent, A. I. 2006, *ApJ*, **646**, 1070
 Artymowicz, P., & Lubow, S. H. 1994, *ApJ*, **421**, 651
 Bai, X.-N., & Stone, J. M. 2013, *ApJ*, **769**, 76
 Barnes, J. E., & Hernquist, L. 1996, *ApJ*, **471**, 115
 Bast, J. E., Brown, J. M., Herczeg, G. J., van Dishoeck, E. F., & Pontoppidan, K. M. 2011, *A&A*, **527**, A119
 Beckwith, S. V. W., Sargent, A. I., Chini, R. S., & Guesten, R. 1990, *AJ*, **99**, 924
 Blandford, R. D., & Payne, D. G. 1982, *MNRAS*, **199**, 883
 Brown, J. M., Pontoppidan, K. M., van Dishoeck, E. F., et al. 2013, *ApJ*, **770**, 94
 Bruderer, S., van der Marel, N., van Dishoeck, E. F., & van Kempen, T. A. 2014, *A&A*, **562**, A26
 Bruderer, S., van Dishoeck, E. F., Doty, S. D., & Herczeg, G. J. 2012, *A&A*, **541**, A91
 Cabrit, S., Pety, J., Pesenti, N., & Dougados, C. 2006, *A&A*, **452**, 897
 Casassus, S., van der Plas, G., M. S. P., et al. 2013, *Natur*, **493**, 191
 Chen, H., Myers, P. C., Ladd, E. F., & Wood, D. O. S. 1995, *ApJ*, **445**, 377
 Christiaens, V., Casassus, S., Perez, S., van der Plas, G., & Ménard, F. F. 2014, *ApJL*, **785**, L12
 Close, L. M., Dutrey, A., Roddier, F., et al. 1998, *ApJ*, **499**, 883
 Corder, S., Eisner, J., & Sargent, A. 2005, *ApJL*, **622**, L133
 de Geus, E. J., Bronfman, L., & Thaddeus, P. 1990, *A&A*, **231**, 137
 D’Onghia, E., Vogelsberger, M., Faucher-Giguere, C.-A., & Hernquist, L. 2010, *ApJ*, **725**, 353
 Dullemond, C. P., & Dominik, C. 2004, *A&A*, **417**, 159
 Dutrey, A., Guilloteau, S., & Guelin, M. 1997, *A&A*, **317**, L55
 Duvert, G., Dutrey, A., Guilloteau, S., et al. 1998, *A&A*, **332**, 867
 Eisner, J. A., Hillenbrand, L. A., White, R. J., Akeson, R. L., & Sargent, A. I. 2005, *ApJ*, **623**, 952
 Ferreira, J., Dougados, C., & Cabrit, S. 2006, *A&A*, **453**, 785
 Gahm, G. F., Walter, F. M., Stempels, H. C., Petrov, P. P., & Herczeg, G. J. 2008, *A&A*, **482**, L35
 Ghez, A. M., Neugebauer, G., & Matthews, K. 1993, *AJ*, **106**, 2005
 Gorti, U., & Hollenbach, D. 2009, *ApJ*, **690**, 1539
 Goto, M., Usuda, T., Takato, N., et al. 2003, *ApJ*, **598**, 1038
 Greene, T. P., Wilking, B. A., Andre, P., Young, E. T., & Lada, C. J. 1994, *ApJ*, **434**, 614
 Günther, R., & Kley, W. 2002, *A&A*, **387**, 550
 Hanawa, T., Ochi, Y., & Ando, K. 2010, *ApJ*, **708**, 485
 Herczeg, G. J., Walter, F. M., Linsky, J. L., et al. 2005, *AJ*, **129**, 2777
 Jørgensen, J. K., Bourke, T. L., Myers, P. C., et al. 2007, *ApJ*, **659**, 479
 Kenyon, S. J., Lada, E. A., & Barsony, M. 1998, *AJ*, **115**, 252
 Klaassen, P. D., Juhasz, A., Mathews, G. S., et al. 2013, *A&A*, **555**, A73
 Knigge, C., Woods, J. A., & Drew, J. E. 1995, *MNRAS*, **273**, 225
 Koresko, C. D. 2002, *AJ*, **124**, 1082
 Kurosawa, R., Harries, T. J., & Symington, N. H. 2006, *MNRAS*, **370**, 580
 Lacy, J. H., Knacke, R., Geballe, T. R., & Tokunaga, A. T. 1994, *ApJL*, **428**, L69
 Liu, M. C., Graham, J. R., Ghez, A. M., et al. 1996, *ApJ*, **461**, 334
 Loinard, L., Torres, R. M., Mioduszewski, A. J., & Rodríguez, L. F. 2008, *ApJL*, **675**, L29
 Mamajek, E. E. 2008, *AN*, **329**, 10
 Mayama, S., Tamura, M., Hanawa, T., et al. 2010, *Sci*, **327**, 306
 McCabe, C., Ghez, A. M., Prato, L., et al. 2006, *ApJ*, **636**, 932
 McMullin, J. P., Waters, B., Schiebel, D., Young, W., & Golap, K. 2007, in ASP Conf. Ser. 376, Astronomical Data Analysis Software and Systems XVI, ed. R. A. Shaw, F. Hill, & D. J. Bell (San Francisco, CA: ASP), **127**
 Melo, C. H. F. 2003, *A&A*, **410**, 269
 Mihos, J. C., & Hernquist, L. 1996, *ApJ*, **464**, 641
 Mundt, R. 1984, *ApJ*, **280**, 749
 Murray, C. D., & Dermott, S. F. 1999, Solar System Dynamics (New York: Cambridge Univ. Press)
 Najita, J., Carr, J. S., & Mathieu, R. D. 2003, *ApJ*, **589**, 931
 Öberg, K. I., Qi, C., Fogel, J. K. J., et al. 2010, *ApJ*, **720**, 480
 Öberg, K. I., Qi, C., Fogel, J. K. J., et al. 2011, *ApJ*, **734**, 98
 Ochi, Y., Sugimoto, K., & Hanawa, T. 2005, *ApJ*, **623**, 922
 Paczynski, B. 1977, *ApJ*, **216**, 822
 Panić, O., Hogerheijde, M. R., Wilner, D., & Qi, C. 2008, *A&A*, **491**, 219
 Panogloiu, D., Cabrit, S., Pineau Des Forets, G., et al. 2012, *A&A*, **538**, A2
 Pichardo, B., Sparke, L. S., & Aguilar, L. A. 2005, *MNRAS*, **359**, 521
 Piétu, V., Gueth, F., Hily-Blant, P., Schuster, K.-F., & Pety, J. 2011, *A&A*, **528**, A81
 Piétu, V., Guilloteau, S., & Dutrey, A. 2005, *A&A*, **443**, 945
 Pontoppidan, K. M., Blake, G. A., & Smette, A. 2011, *ApJ*, **733**, 84
 Pontoppidan, K. M., Meijerink, R., Dullemond, C. P., & Blake, G. A. 2009, *ApJ*, **704**, 1482
 Pontoppidan, K. M., Salyk, C., Blake, G. A., et al. 2010, *ApJ*, **720**, 887
 Prato, L., Greene, T. P., & Simon, M. 2003, *ApJ*, **584**, 853
 Pudritz, R. E., & Norman, C. A. 1983, *ApJ*, **274**, 677
 Pudritz, R. E., Ouyed, R., Fendt, C., & Brandenburg, A. 2007, in Protostars and Planets V, ed. B. Reipurth, D. Jewitt, & K. Keil (Tucson, AZ: Univ. Arizona Press), **277**
 Ray, T., Dougados, C., Bacciotti, F., Eisloffel, J., & Chrysostomou, A. 2007, in Protostars and Planets V, ed. B. Reipurth, D. Jewitt, & K. Keil (Tucson, AZ: Univ. Arizona Press), **231**
 Reipurth, B., & Zinnecker, H. 1993, *A&A*, **278**, 81
 Rigliaco, E., Pascucci, I., Gorti, U., Edwards, S., & Hollenbach, D. 2013, *ApJ*, **772**, 60
 Roddier, C., Roddier, F., Northcott, M. J., Graves, J. E., & Jim, K. 1996, *ApJ*, **463**, 326
 Rosenfeld, K. A., Andrews, S. M., Hughes, A. M., Wilner, D. J., & Qi, C. 2013, *ApJ*, **774**, 16

- Rosenfeld, K. A., Chiang, E., & Andrews, S. M. 2014, *ApJ*, **782**, 62
Rosenfeld, K. A., Qi, C., Andrews, S. M., et al. 2012, *ApJ*, **757**, 129
Salyk, C., Herczeg, G. J., Brown, J. M., et al. 2013, *ApJ*, **769**, 21
Salyk, C., Pontoppidan, K. M., Blake, G. A., et al. 2008, *ApJL*, **676**, L49
Simon, M., Dutrey, A., & Guilloteau, S. 2000, *ApJ*, **545**, 1034
Thies, I., Kroupa, P., & Theis, C. 2005, *MNRAS*, **364**, 961
Wang, H., Mundt, R., Henning, T., & Apai, D. 2004, *ApJ*, **617**, 1191
White, R. J., & Ghez, A. M. 2001, *ApJ*, **556**, 265
Wilking, B. A., Meyer, M. R., Robinson, J. G., & Greene, T. P. 2005, *AJ*, **130**, 1733
Yang, H., Herczeg, G. J., Linsky, J. L., et al. 2012, *ApJ*, **744**, 121
Zhang, K., Pontoppidan, K. M., Salyk, C., & Blake, G. A. 2013, *ApJ*, **766**, 82